**Computers and Concrete**, *Vol. 15, No. 2 (2015) 305-319*
DOI: http://dx.doi.org/10.12989/cac.2015.15.2.305 

# Mesoscale computational simulation of the mechanical response of reinforced concrete members

Licheng Wang*[1,2] and Jiuwen Bao[2b]

[1]*State Key Laboratory of Simulation and Regulation of Water Cycle in River Basin, China Institute of Water Resources and Hydropower Research, Beijing 100038, China*
[2]*State Key Laboratory of Coastal and Offshore Engineering, Dalian University of Technology, Dalian 116024, China*

(*Received November 4, 2013, Revised September 8, 2014, Accepted November 3, 2014*)

**Abstract.** On mesoscopic level, concrete can be treated as a three-phase composite material consisting of mortar, aggregates and interfacial transition zone (ITZ) between mortar and aggregate. A lot of research has confirmed that ITZ plays a crucial role in the mechanical fracture process of concrete. The aim of the present study is to propose a numerical method on mesoscale to analyze the failure mechanism of reinforced concrete (RC) structures under mechanical loading, and then it will help precisely predict the damage or the cracking initiation and propagation of concrete. Concrete is meshed by means of the Rigid Body Spring Model (RBSM) concept, while the reinforcing steel bars are modeled as beam-type elements. Two kinds of RC members, i.e. subjected to uniaxial tension and beams under bending, the fracture process of concrete and the distribution of cracks, as well as the load-deflection relationships are investigated and compared with the available test results. It is found that the numerical results are in good agreement with the experimental observations, indicating that the model can successfully simulate the failure process of the RC members.

**Keywords:** mesoscale simulation; Rigid Body Spring Model (RBSM); reinforced concrete (RC) member; crack distribution; deflection

## 1. Introduction

In terms of the composite structure, concrete should not be looked as a homogeneous material because it is a three-phase composite system consisting of aggregates embedded in a matrix of hardened cement paste, and the interfacial transition zones (ITZs) on the interface between the aggregate particles and the surrounding cement paste (Oh and Jang 2004, Caré and Hervé 2004, Sadouki and Van Mier 1997, Zhou and Hao 2008). This description of concrete is widely recognized and usually defined as mesoscale approach, which is specifically useful when analyzing the influence of the aggregates and the ITZs on the mechanical properties of concrete, particularly on fracture behavior, as well as on the transport processes (Guinea *et al*. 2002, Wang and Ueda 2011). Therefore, over the past few years, the numerical analysis of concrete on

∗Corresponding author, Associate Professor, E-mail: wanglicheng2000@163.com
[a]Ph.D., E-mail: wanglicheng2000@163.com
[b]Ph.D. Student, E-mail: baojiuwen55@126.com


http://www.techno-press.org/?journal=cac&subpage=8 ISSN: 1598-8198 (Print), 1598-818X (Online)

mesoscale has been successfully conducted, leading to a better understanding of the micro-cracking and fracture behavior of concrete (Cusatis *et al*. 2003, Jirásek and Grassl 2008, Grassl and Jirásek 2010, Grassl and Rempling 2008). Moreover, the mesoscopic analysis can represent the effects of aggregates shape, distribution and volume fraction, particularly the thickness and properties of the ITZ (Kim and Abu Al-Rub 2011).

However, the majority of the conducted studies are focused on the mechanical simulation of plain concrete due to the computational complexity and cost after including the reinforcement. To well extend the application of mesoscopic type approach to structural analysis, the reinforcement should be firstly introduced into the model. Therefore, the objective of this study is to develop a meso-mechanical approach to investigate the response of RC members subjected to uniaxial tension or bending load. In this method, the two-dimensional (2D) mesoscale geometry of concrete is meshed by the Voronoi diagram and the discrete element method, named Rigid Body Spring Model (RBSM), is adopted to perform the mechanical analysis. The advantage of the Voronoi diagram is that it can reduce mesh bias on potential crack directions because the crack initiation and propagating direction have been prescribed in advance. The continuous reinforcement is dispersed irrespective of the diagram of the concrete Voronoi meshing. Each reinforcing element is regarded as a general beam element. A specific link element with zero-size is used to simulate the bonding behavior between reinforcement and concrete. The proposed model is applied to the RC members who have been experimentally studied in order to verify the feasibility and efficiency of the method.

## 2. General description of the basic models

### *2.1 Concept of the RBSM*

In the currently developed method, concrete is represented by the RBSM theory on mesoscale level. In terms of the RBSM approach, the domain of sample geometry is meshed into polyhedron elements whose common boundary segments are assumed to be interconnected by zero-size springs, using a Voronoi diagram based on a set of randomly distributed points. Each element has two translational and one rotational degree of freedom for a 2D case (Fig. 1). The elastic modulus of the springs as shown in Fig. 1 can be written as follows when a plane stress condition is assumed:

$$k_{\mathrm{ne}} = \frac{E_{\mathrm{elem}}}{\left(1-\nu_{\mathrm{elem}}{}^{2}\right)}$$
$$k_{\mathrm{te}} = \frac{E_{\mathrm{elem}}}{1+\nu_{\mathrm{elem}}} \tag{1}$$

where $k_{\mathrm{ne}}$ and $k_{\mathrm{te}}$ are the elastic moduli of normal and shear springs respectively; $E_{\mathrm{elem}}$ and $\nu_{\mathrm{elem}}$ are the calibrated elastic modulus and Poison's ratio of element on the mesoscale level, respectively.

The response of the springs can simulate the interaction between elements instead of considering the internal behavior of each element. This has been regarded as the most significant feature of the discrete element method, for example the RBSM. The mechanical properties of springs are assigned with different characteristic depending on their position (i.e. in the aggregate,

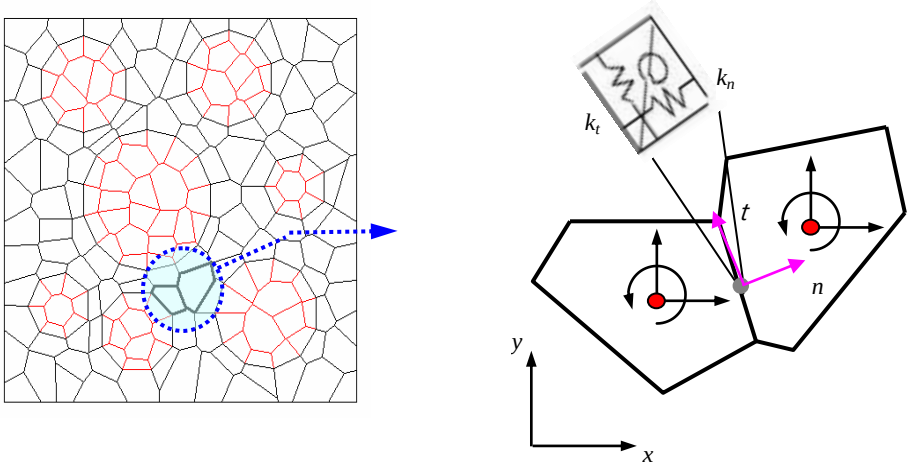


Fig. 1 RBSM mechanical model

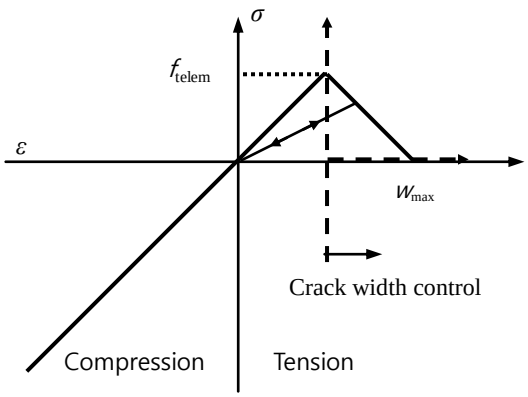


Fig. 2 Constitutive model of the normal spring (Nagai et al. 2004)

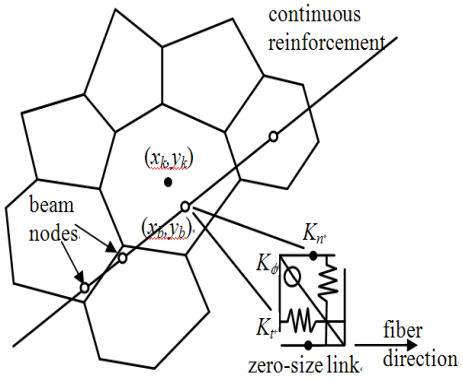


Fig. 3 Beam elements of steel bar embedded in the Voronoi diagram of concrete

mortar, interface or macro concrete element). In terms of the heterogeneity of concrete material, the mechanical parameters, including the strength and elastic modulus, are assumed to follow normal distribution, which is used to account for the randomness of material damage and localization. The probability density function for the tensile strength of mortar is written as

$$\begin{aligned} f(f_{telem}) &= \frac{1}{\sqrt{2\pi}\sigma}\exp\{-\frac{(f_{telem}-\mu)^2}{2\sigma^2}\} \\ \mu &= f_{taverage} \\ \sigma &= -0.2 f_{telem} + 1.5 \end{aligned} \tag{2}$$

in which $f_{telem}$ is the distributed tensile strength and $f_{taverage}$ is the average tensile strength of mortar on the mesoscale. When $f_{telem}$ is less than 0, $f_{telem}$=0.

Both the normal and shear springs behave elastically until the stresses reach the tensile strength

or the maximum shear stress criterion. In the paper, only the constitutive model of a normal spring is depicted in Fig. 2. The formulation for the maximum shear stress criterion can be referred to Nagai *et al*. (2004).

Only a short overview of RBSM on mesoscale of concrete is given above. Additional details, such as those related to element meshing process and constitutive laws of different phases of concrete have been reported in literatures (Nagai *et al*. 2004 and Wang *et al*. 2008).

### *2.2 Steel element*

For a RC specimen, the continuous steel bars are overlapped on the Voronoi diagramming geometry ignoring the layout of concrete elements. It implies that that the reinforcing bar trajectories are independent of the geometry of the Voronoi elements representing the concrete, which greatly facilitates the model construction and revision. Each reinforcing bar is represented by a series of regular beam elements, as shown in Fig. 3. Given the bar trajectory, beam end nodes are set to be located midway along the pathway traversing each Voronoi cell. By this manner, the number of beam-column elements is proportional to the average density of Voronoi element (Bolander and Le 1999). The interactions between reinforcement and concrete can be realized via zero-size link elements (see Fig. 3). The spring parallel to the reinforcing bar (with stiffness of $K_t$) represents the bond action between the bar and the concrete material, which will be described by the nonlinear stress-slip relation in the followed section. Much large stiffnesses ($K_n$ and $K_\phi$) are assigned to the normal and rotational springs of the link element because the relative displacements for these two component directions are almost nil (Bolander *et al*. 2000).

One of the link nodes is attached to the beam node (e.g. the node with coordinate of $x_b$ and $y_b$ in Fig. 3), while the motion of the other link node is rigidly constrained to the associated Voronoi node of ($x_k$, $y_k$). This strategy has already been applied to the numerical simulation of RC structures on macroscopic level in terms of RBSM (Bolander and Saito 1998, Bolander and Hong 2002, Nakamura *et al*. 2006).

After prescribing the position and direction of steel rebar, the end nodes of a beam element can be automatically generated along the path traversing each Voronoi element, as shown in Fig. 3. Assuming small rotations, the displacement ($u_1$, $v_1$) of a beam node ($x_b$, $y_b$) will move with the gravity center of concrete element ($x_k$, $y_k$) with motion equation as

$$\begin{aligned} u_1 &= u - (y_b - y_k)\theta \\ v_1 &= v - (x_b - x_k)\theta \end{aligned} \tag{3}$$

in which $u$, $v$, $\theta$ represent the two translational displacements and the rotational displacement, respectively. The relative displacements between the two link nodes are given by $\mathbf{d}=\mathbf{Bu}$, where

$$\mathsf{B} = \begin{bmatrix} -1 & 0 & (y_b - y_k) & 1 & 0 & 0 \\ 0 & -1 & -(x_b - x_k) & 0 & 1 & 0 \\ 0 & 0 & -1 & 0 & 0 & 1 \end{bmatrix} \tag{4}$$

and $\mathbf{u}^T=[u,v,\theta,u_1,v_1,\theta_1]$ are the generalized displacement components of the computational point and the beam node, respectively; $\mathbf{d}^T=[\delta_n,\delta_t,\phi]$ are the normal, tangential and rotational

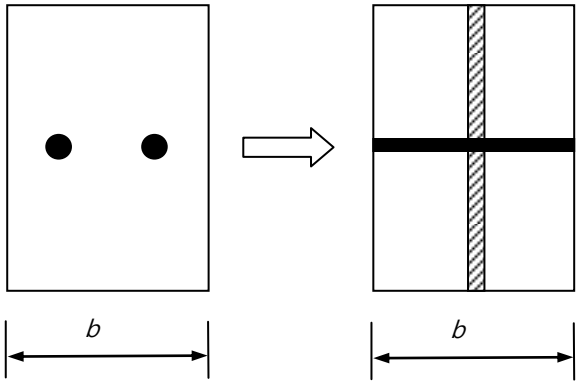


Fig. 4 Illustration of conversion method for the cross-sectional area of reinforcements

displacements, respectively. To obtain relationship between the local and global coordinate, the transformation matrix is required with expression as following

$$\mathbf{T}=\begin{bmatrix}\cos\alpha & \sin\alpha & 0\\ -\sin\alpha & \cos\alpha & 0\\ 0 & 0 & 1\end{bmatrix} \tag{5}$$

in which $\alpha$ is the angle between the reinforcement and the horizontal coordinate. Thus, the stiffness matrix of the link element can be written as

$$\mathbf{K}_{\mathrm{e}}=\mathbf{B}^{T}\mathbf{T}^{T}\mathbf{DBT} \tag{6}$$

where **D** is a diagonal matrix containing the normal, tangential, and rotational spring stiffness of the previously described springs as given by

$$\mathbf{D}=\begin{bmatrix}k_n & 0 & 0\\ 0 & k_t & 0\\ 0 & 0 & k_\phi\end{bmatrix} \tag{7}$$

In the diagonal matrix **D**, $k_n$, $k_t$, $k_\phi$ are the normal, tangential and rotational stiffness of the link springs, respectively.

In order to reduce the computing burden, the real 3-dimensional specimen is simplified into a 2-dimensional (2D) model. In the 2D configuration, the aggregate size and grading can be generated with the Fuller equation proposed by Walraven and Reinhard (1981). In terms of the reinforcing bar, the area of $n$ bars on the same height (with diameter of $d$) is assumed to uniformly distribute on the width direction. Therefore, for the 2D simulation, if the thickness of a sample is set as unit value, the cross-sectional area of steel reinforcement ($A_s$) can be calculated by $A=n\pi d^2/4b$, in which $b$ is the width of the specimen section. This conversion method is illustrated by Fig. 4.

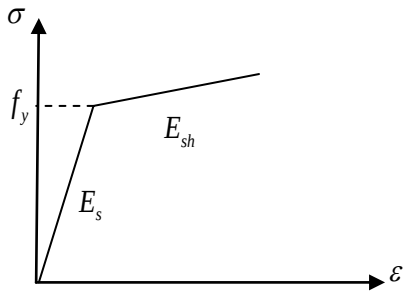


Fig. 5 Stress-strain relationship of reinforcement under loading

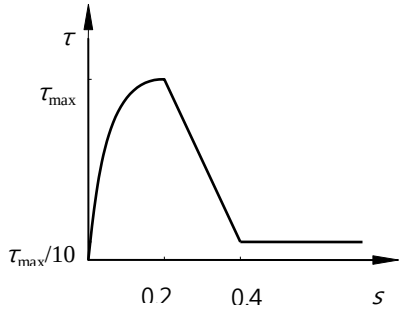


Fig. 6 Bond-slip relationship of the reinforcement within concrete

### *2.3 Constitutive model of the reinforcement*

The bilinear stress-strain relationship, as shown in Fig. 5, is applied to the beam element of steel reinforcement. The elastic modulus of the strengthened branch, $E_{sh}$, is taken as the 1% of the initial elastic modulus of steel.

It is evident that the interaction between reinforcement and concrete has a great influence on the crack formation and propagation. As a result, it is desirable to take into account the bond stress-slip relationship. In this study, the spring parallel to reinforcing bar is used to represent this bond action between the bar and the concrete material. The strength and stiffness of the spring aligned tangentially to the bar are governed by non-linear stress-slip relations determined through experimentation, for example the model developed by Shima *et.al*. (1987) (as given in Fig. 6).

The formulation for the ascending branch of stress-slip relationship in Fig. 6 is written as follows (Nakamura *et al*. 2006):

$$\tau = \gamma 0.9 f_c'^{2/3} \left(1 - \exp(-10(s/d)^{1/2})\right) \qquad \text{for} \quad s \le 0.2 \tag{8}$$

where $s$ is the slip between reinforcing bar and concrete; $f_c'$ is the compressive strength of concrete; $d$ is the steel diameter; $\gamma$ is a reduction coefficient. Eq. (8) is only applicable to the mass concrete and the effect of concrete cover should be taken into account when it is used for the beam case because of its mush thinner cover thickness compared to mass concrete. In this paper, $\gamma$ =0.6. In addition, the bond strength between concrete and reinforcement in the numerical simulations below, $\tau_{max}$, is calculated as 5.59 MPa by Eq. (8) when the slip $s$=0.2 mm.

## 3. RC beam under bending -Verification I

### *3.1 Construction of the numerical models*

In this section, the four-point bending beam, which has been experimentally studied by Revathi and Menon (2005), is numerically analyzed to simulate its mechanical response and to compare with test observations. The compressive strength of concrete is 20 MPa, and the yield strengths of

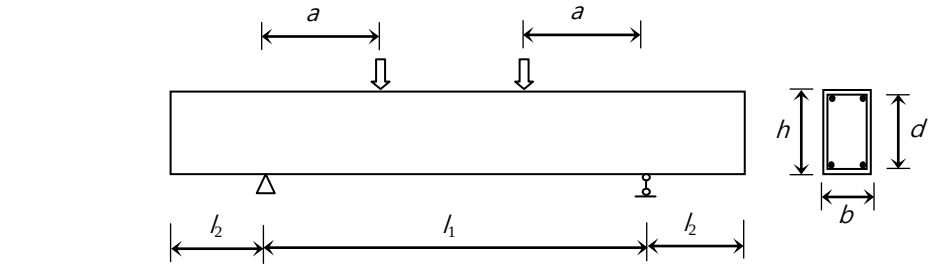


(a) Loading mode (Unit: mm)

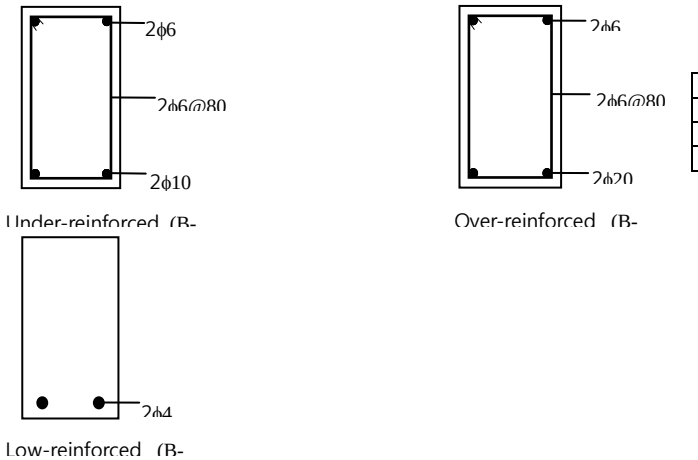


| | $l_1$ | $l_2$ | $a$ | $b$ | $h$ | $d$ |
|---|---|---|---|---|---|---|
| B-1 | 1800 | 100 | 600 | 150 | 200 | 160 |
| B-2 | 1800 | 100 | 600 | 150 | 200 | 160 |
| B-3 | 1500 | 250 | 500 | 120 | 200 | / |

(b) Reinforcement details of specimens (c) Specimens size

Fig. 7 Configuration and loading mode of the RC beams

(a) Under-reinforced or over-reinforced (b) Low-reinforced

Fig. 8 Numerical simulation models

Table 1 Mechanical parameters of the materials on mesoscale

| Type | Young's modulus $E$/GPa | Poisson ratio $\mu$ | Tensile strength $f_t$/MPa |
|---|---|---|---|
| Aggregate | 50.0 | 0.25 | 6 |
| Mortar | 23.6 | 0.18 | 3.50 |
| ITZ | 20.9 | 0.15 | 1.15 |
| Concrete | 25.98 | 0.2 | 1.94 |
| Longitudinal rebars | 200 | / | 415 |
| Stirrups | 200 | / | 250 |

tensile reinforcement and stirrup are 415 and 250 MPa respectively. The Young's moduli of steel bars and concrete are $2\times10^5$ and 25980 MPa, respectively. The shape, dimensions, loading point

locations, and reinforcement details of specimens used in the experiments are shown in Fig. 7. In the current numerical analysis, the incremental displacement of 0.02 mm is applied on the two loading points.

The numerical model of the specimen after meshed with the Voronoi diagram is shown in Fig. 8. The one-third lengths of the beam on both right and left hand parts are discretised by using the macroscale elements, but the middle zone is meshed in terms of the mesoscale modeling of concrete composition so that the time of model building and computing can be reduced greatly. The number of concrete elements in Fig. 8(a) is 2729 with an average element size of 12.6mm. For the low-reinforced beam, the point locations and reinforcement details of specimens used in the experiments differ from the under-reinforced or over-reinforced one so that 2661 concrete elements with an average element size of 12.3mm are employed. Here and elsewhere in the paper, the average element size is estimated through dividing the sample length by element numbers in the longitudinal direction. The material parameters are listed in Table 1. A displacement loading mode will be applied. In other words, in each calculation step two equal displacements are symmetrically exerted on the points of the mid-span of the beam in order to obtain a pure bending segment. During the computing process, the convergence condition is judged and the displacement increment will be preceded to next step when the square root of the sum-of-squared-error between the current and former steps becomes less than $10^{-5}$ or the iterative times are larger than a specified maximum value. When the load-defection curve switches to the descending branch, running of the program may be ended at a given percentage of peak loads.

### *3.2 Under-reinforced beam*

The numerically simulated load-deflection curve for the under-reinforced beam with the present method is compared with the test results in Fig. 9. While not perfect, a relatively good agreement can be observed. The peak load and its corresponding deflection at the mid-span are 41.12 kN and 11.67 mm. The two measurements of test result are 38 kN and 12.39 mm, respectively. Also, from Fig. 9 it can be seen that both the beams from numerical simulation and test undergo three distinct stages before it failed by the load. However, after loading 20 kN, the load of numerical simulation on load-deflection curve increases faster than that of the test curve. This result may be attributed to the two reasons: i) the constitutive laws of shear and rotational springs on the common boundary of Voronoi elements of concrete may be too idealistic; ii) the other one may be that the error induced by the actual test makes the bearing capacity lower. Nevertheless, the existed difference between numerical simulation and test result can be acceptable. The above analysis can illustrate the possibility to use the currently proposed numerical method for simulating the mechanical behavior of reinforced concrete structures.

The cracking pattern and distribution with three different mid-span deflections are depicted in Fig. 10. It can be noted that, for the under-reinforced beam, cracks of concrete mainly present in the mid-span region. Fig. 11 demonstrates the steel stress distribution along the longitudinal direction under various mid-span deflections. It can be seen that when the mid-span defection is 2.24 mm, the steel stress reaches 150 MPa (lower than the yield strength of 415 MPa) and tends to be slightly higher at position of the four principal cracks (see Fig. 10(a)). Furthermore, when the mid-span deflection is increased to 5.69 mm, the steel bars begin to yield. After this point, the increase of steel stress is marginal, which results in a flat phase on the load-defection curve. The stiffness of the beam in this stage is significantly weakened and from Fig. 9, a large increase of the deflection (almost 10 mm) was observed. In addition, from Fig.10, one can find that the number of

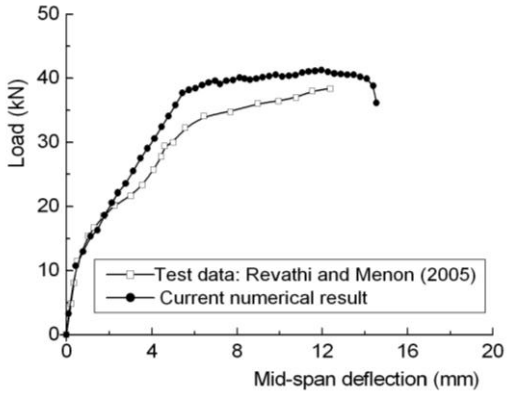


Fig. 9 Load-deflection curve of the under-reinforced beam

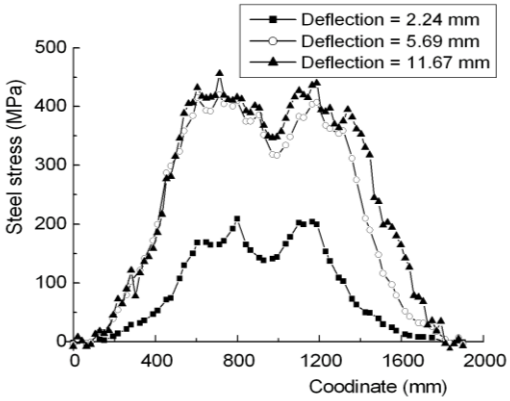


Fig. 11 Steel stress distribution along the longitudinal direction

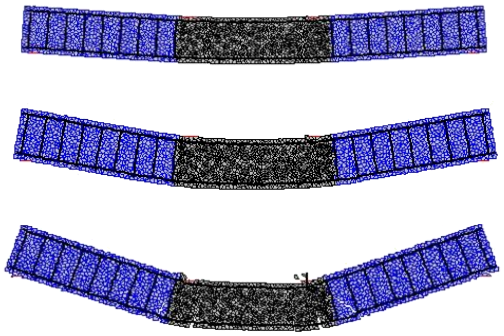

(a) Mid-span deflection = 2.24mm (Load = 21.32kN)

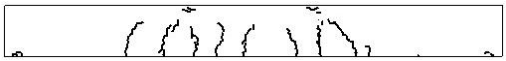

(b) Mid-span deflection =5.69mm (Load = 38.07kN)

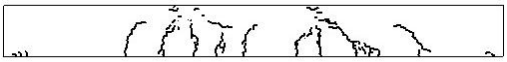

(c) Mid-span deflection = 11.67 mm (Load = 41.12kN)

Fig. 10 Propagation and distribution of the cracks for under-reinforced beam

principal cracks in the middle zone (also called the pure bending segment) keeps unchanged after yielding of the longitudinal steel bars. The mean crack spacing is around 130 mm in this example.

### *3.3 Over-reinforced beam*

Employing the same numerical analysis approach, the load-deflection curve for the over-reinforced beam is shown in Fig. 12 to be compared with test result. The ultimate load from numerical data is about 82kN, which is smaller than that measured in test (90kN). Because no descending branch was recorded in the test, it became difficult to estimate the deflection corresponding to the peak load. However, from the viewpoint of approximation, the two curves in Fig. 12 match well on the whole. The fracture patterns, including the propagation and distribution of cracks, obtained at two stages of the analysis are shown in Fig. 13. Compared with the under-reinforced beam, the cracks presenting in the mid-span zone develop much more slowly and their propagating heights are lower. At the peak load point, a large number of cracks are found in the pure bending zone, but they are finer. Therefore, as would be expected, the average crack width is much smaller than that arising in the under-reinforced beam. Likewise, the steel stress distributions

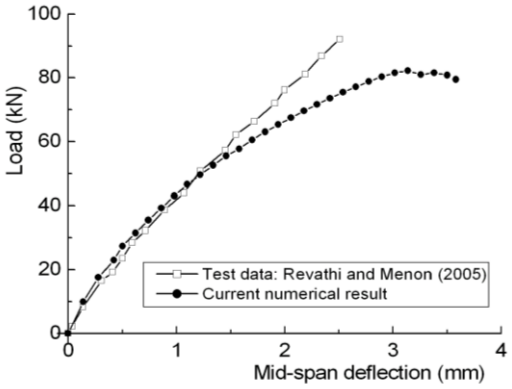


Fig. 12 Load-displacement curve of over-reinforced beam

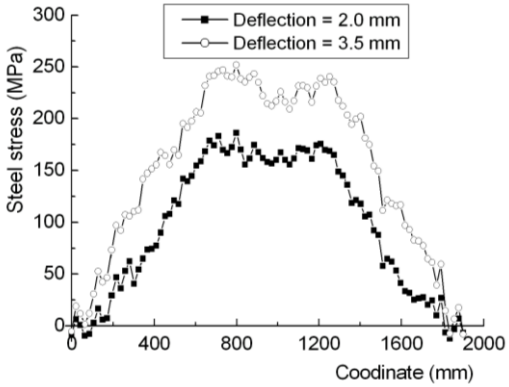


Fig. 14 Stress of the steel bar in the over-reinforced beam

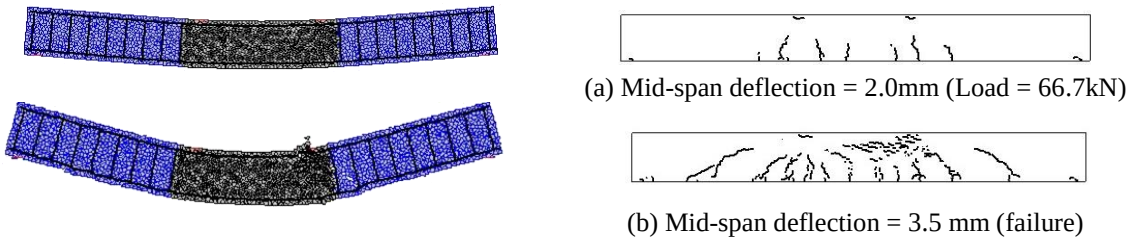

(a) Mid-span deflection = 2.0mm (Load = 66.7kN)

(b) Mid-span deflection = 3.5 mm (failure)

Fig. 13 Propagation and distribution of the cracks

are acquired and plotted in Fig. 14. The maximum steel stress corresponding to the peak load is about 251 MPa, which is far below the yielding strength of the steel bars, i.e. 415 MPa as given in Table 1. These observations are in general agreement with some preliminary conclusions drawn for the failure mode of over-reinforced concrete beams.

### *3.3 Model verification*

With these models and input parameters, the numerical results are compared with the experimental results as shown in Figs. 5(a)-(f), which indicates that the calculated displacement of unconfined columns is slightly smaller than the measured one. This is mainly due to neglecting the slip between the steel bars and concrete in the numerical analysis. The larger stiffness difference between the numerical and experimental hysteretic loops shown in Fig. 5(a) could be induced by experimental errors.

The difference in the descending branch between the numerical and experimental results shown in Figs. 5(d)-(f) is due to the constitutive model of concrete adopted in OpenSees. As shown in Fig. 12(a), the constitutive model of CFRP confined concrete is approximated by projecting the stresses and strains at points A and B onto the unconfined concrete model. However, there exists a residual stiffness after point B in the Kent-Park model. In addition, the difference could be also induced by neglecting the slip between the steel bars and concrete.

As shown in Table 7, the calculated bearing capacity $P_{num}$ is higher than the measured one $P_{exp}$, but the difference is smaller than 10%. Although there are slight differences between the calculated

and measured hysteretic loops, the numerical results are still in good agreement with the experimental results.

### *3.4 Low reinforced beam*

Low reinforced beam is usually referred to that failure of the beam occurs immediately after cracking of the concrete. The reason is that the so much small reinforcement is unable to carry the force released by cracking of the concrete. Therefore, the ultimate carrying capacity of a low reinforced beam is theoretically no more than the cracking load. The load-deflection curves of the low reinforced beams, including the test data and numerical result, are shown in Fig. 15. It can be seen that the cracking load is almost same as that of the under-reinforced beam. Before cracking, the curves obtained from numerical simulation and test results agree well to each other. However, after cracking, they begin to deviate gradually. The test curve exhibits constant load but rapid increase of deflection. The numerical curve regains growth with a much lower slope compared with the initial stage. The failure modes and cracking distributions obtained from numerical analysis and test are given in Fig. 16. In the test, only one principal crack is observed, which almost extends to the top surface of the beam. But for the case of numerical simulation, there are two apparent cracks presenting in the pure bending segment. This may be attributed to the influence of the bond-slip relationship between concrete and the steel bars. In the test study, plain round bars were used, which have very poor bond performance with concrete. On the contrary, Eq. (8) was experimentally obtained by means of the deformed steel bars.

The steel stress distributions are shown in Fig. 17 corresponding to the mid-span deflection of 0.57 mm and 4.0 mm respectively. It can be seen that when the mid-span deflection is 4.0 mm, the

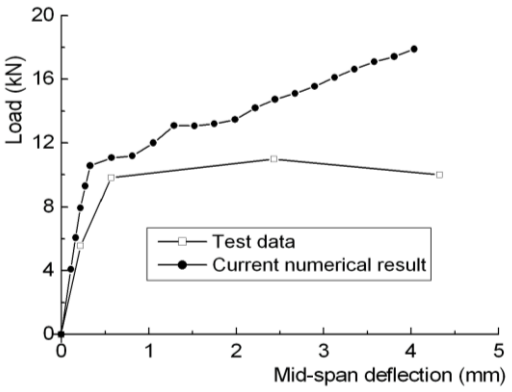


Fig. 15 Load-displacement curve of the lower-reinforced beam

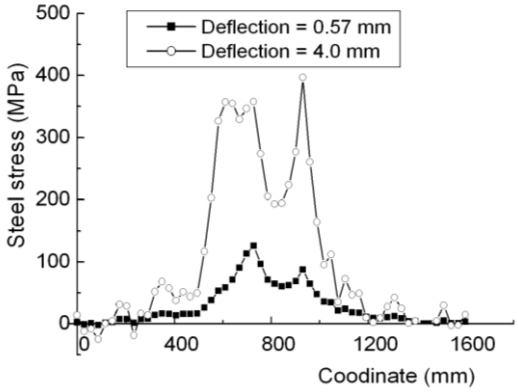


Fig. 17 Stress distribution of the steel bar at bottom of the over-reinforced beam

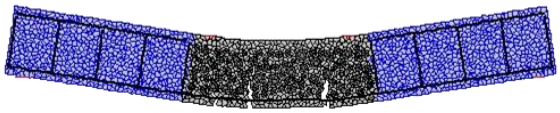

(a) Numerical simulated result

(b) Test photo

Fig. 16 Failure model of the lower-reinforced beam

steel stress at the crack position has run up to 400 MPa. This value is beyond the yielding strength of the reinforcement, indicating the steel bars have entered the strain-hardening stage. This is one of the main mechanisms which result in the continued, but lower rate increase of load in the second phase of the numerical load-deflection curve, as shown in Fig. 15.

## 4. Numerical modeling on RC member under uniaxial tensile loading

The RC member shown in Fig. 18 is chosen as the numerical example to demonstrate the analysis procedure of the proposed model. The size of the specimen is 300 mm×100 mm×100 mm and aggregate volume fraction is 32.5% by area. Only one centrically positioned rebar with diameter of 12 mm is considered. The mechanical parameters for calculation are listed in Table 2.

The specimen meshed by Voronoi diagram is shown in Fig. 19 with total 6930 elements, including concrete element and beam element of steel. The left side of the model is set as the fixed boundary and the displacement loading is applied on the right end of steel bar with an increment of 0.001 mm.

The cracking development during loading process is presented in Fig. 20. In order to make the cracks visibly clearer, the deformation is enlarged 20 times along both vertical and horizontal directions. The lower pictures present the simulated cracks corresponding to the upper ones, without showing aggregates in order to clearly reveal the initiation and propagation process of cracks. It can be seen that the shape and distribution of cracks are quite close to those observed in experiments. Additionally, the cracking in specimen firstly initiates on the interface of the coarse aggregates, and then propagates around surface of the aggregate. With increase of the applied displacement, the cracks begin to extend into the mortar matrix and form a connecting network. From Fig. 21, it can also be noted that the crack opening width on surface of the specimen is larger than that at the location of steel reinforcement.

The variation of steel stress along the longitudinal reinforcement is shown in Fig. 21 under different applied displacements on the right end. The effect of concrete cracking is obviously observed.

Table 2 Mechanical parameters of the materials on mesoscale

| Type | Young's modulus $E$/GPa | Poisson ratio $\mu$ | Tensile strength $f_t$/MPa |
|---|---|---|---|
| Aggregate | 50.0 | 0.25 | 300 |
| Mortar | 23.6 | 0.18 | 3.50 |
| ITZ | 21.6 | 0.16 | 1.74 |
| Reinforcement | 210 | / | 300 |

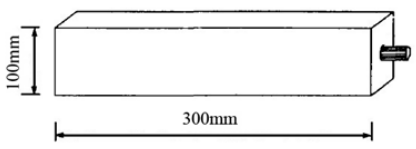


Fig. 18 Configuration of the RC specimen for tensile loading

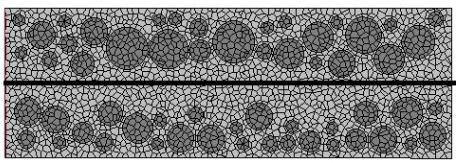

Fig. 19 The 2D Voronoi diagram of the specimen under tensile loading

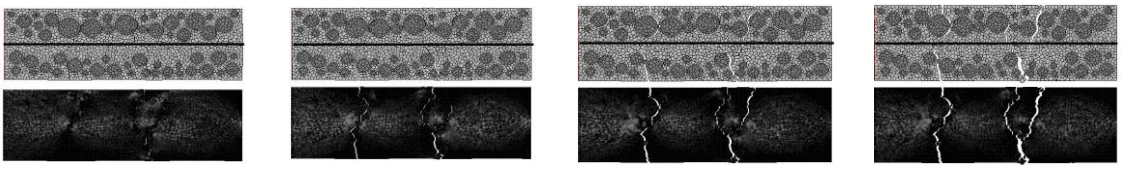

(a) Displacement = 0.2 mm (b) Displacement = 0.5 mm (c) Displacement = 1.0 mm (d) Displacement = 1.5

Fig. 20 Cracking development and distribution of concrete under tensile loading

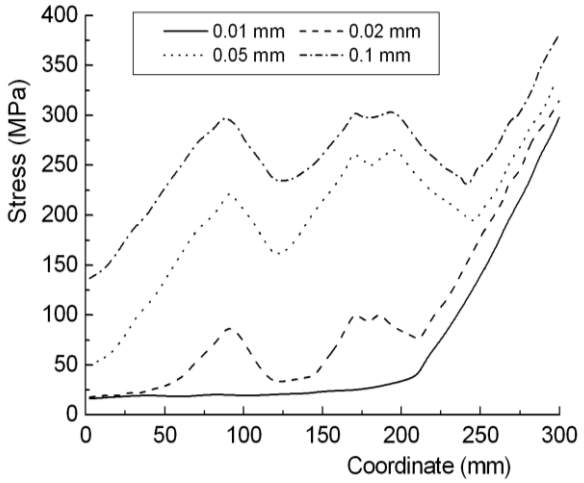


Fig. 21 Steel stress distribution along the longitudinal direction

## 5. Conclusions

A numerical model to simulate the mechanical response of RC structures on mesoscale level of concrete composite is proposed in the current study. In this method, the concrete and steel reinforcements are respectively represented by the Rigid Body Spring Model (RBSM) and the beam elements, which are combined by the zero-size link elements. The failure process of RC members subjected to tensile or bending load were simulated and compared with the available test results. The following conclusions can be drawn:

- On mesoscale, concrete can be regarded as an composite consisting of coarse aggregate, mortar and the interfacial transition zone between the aggregates and mortar in terms of the mechanical properties of each phase and the cracking potential among these components. The method of including reinforcement into concrete model is practical to describe the role of strengthening effect of steel bars and the interaction between concrete and steel.
- The model can successfully simulate the failure process of the RC members. The distribution of cracks within the specimen, as well as the stress distribution of steel bars along their longitudinal direction is well demonstrated under various loading levels. It is shown that the

numerical results are in good agreement with the experimental observations in terms of the failure mode and the load-deformation curves.

## Acknowledgments

This work was financially supported by the National Key Basic Research Program of China (973 Program) (No. 2015CB057703), the Open Research Fund of State Key Laboratory of Simulation and Regulation of Water Cycle in River Basin (China Institute of Water Resources and Hydropower Research) (IWHR-SKL-201309) and the National Natural Science Foundation (No. 51378090) . Their support is gratefully acknowledged.

## References

Bolander, J.E. and Saito, S. (1998), "Fracture analyses using spring networks with random geometry", *Eng. Fract. Mech.*, **61**(5-6), 569-591.

Bolander, J.E. and Le, B.D. (1999), "Modeling crack development in reinforced concrete structures under service loading", *Constr. Build. Mater.*, **13**(1-2), 23-31.

Bolander, J.E., Hong, G.S. and Yoshitake, K. (2000), "Structural concrete analysis using rigid-body-spring networks", *Computer-aided Civ. Infrastruct. Eng.*, **15**(2), 120-133.

Bolander, J.E. and Hong, G.S. (2002), "Rigid-body-spring network modeling of prestressed concrete members", *ACI Struct. J.*, **99**(15), 595-604.

Caré, S. and Hervé, E. (2004), "Application of an n-phase model of the diffusion coefficient of chloride in mortar", *Transport Porous Med.*, **56**(2), 119-135.

Cusatis, G., Bazant, Z.P. and Cedolin, L. (2003), "Confinement-shear lattice model for concrete damage in tension and compression: I. theory", *J. Eng. Mech.*, **129**(12), 1439-1448.

Grassl, P. and Jirásek, M. (2010), "Meso-scale approach to modelling the fracture process zone of concrete subjected to uniaxial tension", *Int. J. Solid. Struct.*, **47**(7-8), 957-968.

Grassl, P. and Rempling, R. (2008), "A damage-plasticity interface approach to the mesoscale modelling of concrete subjected to cyclic compressive loading", *Eng. Fract. Mech.*, **75**(16), 4804-4818,.

Guinea, G.V., El-Sayed, K., Rocco, C.G., Elices, M. and Planas, J. (2002), "The effect of the bond between the matrix and the aggregates on the cracking mechanism and fracture parameters of concrete", *Cement Concrete Res.*, **32**(12), 1961-1970.

Jirásek, M. and Grassl, P. (2008), "Evaluation of directional mesh bias in concrete fracture simulations using continuum damage models", *Eng. Fract. Mech.*, **75**(8), 1921-1943.

Kim, S.M. and Abu Al-Rub, R.K. (2011), "Meso-scale computational modeling of the plastic-damage response of cementitious composites", *Cement Concrete Res.*, **41**(3), 339-358.

Nagai, K., Sato, Y. and Ueda, T. (2004), "Mesoscopic simulation of failure of mortar and concrete by 2D RBSM", *J. Adv. Concrete Tech.*, **2**(3), 359-374.

Nakamura, H., Srisoros, W., Yashiro, R. and Kunieda, M. (2006), "Time-dependent structural analysis considering mass transfer to evaluate deterioration process of RC structures", *J. Adv. Concrete Tech.*, **4**(1), 147-158.

Oh, B.H. and Jang, S.Y. (2004), "Prediction of diffusivity of concrete based on simple analytic equations", *Cement Concrete Res.*, **34**(3), 463-480.

Revathi, P. and Menon, D. (2005), "Nonlinear finite element analysis of reinforced concrete beams", *J. Struct. Eng.*, **32**(2), 135-137.

Sadouki, H. and Van Mier, J.G.M. (1997), "Meso-level analysis of moisture flow in cement composites using a lattice-type approach", *Mater. Struct.*, **30**(10), 579-587.

Shima, H., Chou, L. and Okamura, H. (1987), "Bond-slip-strain relationship of deformed bars embedded in massive concrete", *Concrete Library, JSCE*, (10), 79-94.
Wang, L.C. and Ueda, T. (2011). "Mesoscale modeling of water penetration into concrete by capillary absorption", *Ocean Eng*., **38**(4), 519-528.
Wang, Z.L., Lin, F. and Gu, X.L. (2008), "Numerical simulation of failure process of concrete under compression based on meso-scale discrete element model", *Tsinghua Sci. Tech*., **13**(S1), 19-25.
Walravent, J.C. and Reinhard, H.W. (1981), "Concrete mechanic. part A: theory and experiments on the mechanical behavior of cracks in plain and reinforced concrete subject to shear loading", *Heron*, **26**(1A), 1-68.
Zhou, X.Q. and Hao, H. (2008), "Mesoscale modelling of concrete tensile failure mechanism at high strain rates", *Comput. Struct*., **86**(21-22), 2013-2026.

*CC*